DOI: 10.15480/882.9318

Eighth International Symposium on Marine Propulsors
smp'24, Berlin, Germany, March 2024

Assessing the Influence of the Running-in Phase in Ship's Stern Tube Bearings on Wear Development during Ice Collision Loads

Ahmed Saleh[1], Markus Gilges[1], Benjamin Lehmann[1], Georg Jacobs[1]

[1]Institute for Machine Elements and Systems Engineering, RWTH Aachen University, Aachen, Germany

ABSTRACT

Climate change causes increasing ship activity in polar regions, leading to more frequent propeller-ice collisions. These collisions result in extreme impulse loads on aft stern tube bearings, potentially causing bearing wear and failure. Existing studies often overlook variations in bearing surface roughness and contours during the running-in phase, leading to incorrect mixed-friction regime calculations. This study presents a new approach to calculate running-in wear in the aft stern tube bearings of the research vessel SA Agulhas II. It combines downscaled experiments and numerical simulations to determine post-running-in phase surface roughness. The study reveals the significant influence of the running-in phase on wear risk of the bearing, especially for operating conditions near the transition from mixed to fluid friction regimes. However, for operating conditions causing severe mixed-friction regimes, the influence of the running-in phase on the wear risk is minimal. The highest wear risk occurs for rotational speeds of 90-100 rpm and ice-induced propeller torques of 650-700 kNm. This wear risk assessment can serve as a foundation for operator guidance and maintenance plans to ensure safe vessel operation in ice-covered waters.

Keywords

Stern tube bearings; Wear model; Running-in phase; Elasto-hydrodynamic simulation (EHD); Bearing down scaling.

1 INTRODUCTION

Ship traffic in both polar regions has been increasing during the last few years. In the Arctic Sea, novel commercial shipping routes are developing as the sea ice extent keeps decreasing (Sugimura et al. 2021). In the Antarctic Sea, touristic activities are growing rapidly at the same time (Frame et al. 2022). Growing ship traffic in ice-covered waters leads to more frequent collisions between ship propellers and sea ice which causes significant and stochastic axial and lateral loads on the propeller (Hagesteijn et al. 2012). High lateral (radial) propeller loads are a major cause of damage to the journal bearings (sliding bearings) of propeller shafts, especially to the bearing closest to the propeller (aft stern tube bearing) (Vartdal et al. 2009). For aft stern tube bearings (hereafter referred to as *aft bearings*), the number of cases of bearing wear have increased during the last years (DNV, 2022). To ascertain whether propeller-ice contact contributes to the escalating bearing wear damages, the influence of ice-induced lateral propeller loads on contact and lubrication conditions in the bearings needs to be investigated, including the potential transition to a mixed lubrication (mixed friction) regime. In the case of lubricated contacts, and especially for sliding bearings, the Stribeck curve, as shown in Figure 1, provides a comprehensive representation of the contact and lubrication conditions as a function of speed (Sander et al. 2016). It covers the entire spectrum of lubrication types, ranging from boundary and mixed friction to hydrodynamic lubrication (hydrodynamic friction) in bearings (He et al. 2017). The mixed lubrication regime (see Figure 1) delineates the transition between two distinct lubrication regimes: pure hydrodynamic lubrication, where a fluid fully separates the contacting surfaces, and boundary lubrication, where direct asperity contact predominates. Mixed lubrication regime is thus characterized by the partial separation of adjacent surfaces by the fluid film, allowing interactions between individual surface asperities (Sander et al. 2016, Spikes 1997).

Besides the beginning and end of motion, mixed-friction conditions in the aft bearing can occur due to the magnitude and orientation of ice-induced lateral loads, as well as variations in the rotational speed of the propeller shaft and the oil temperature within the bearings (Lehmann et al. 2022). Although rotational shaft speed and oil temperature can usually be derived from standard condition monitoring systems of modern vessels, ice-induced lateral propeller loads are quite complicated to determine.

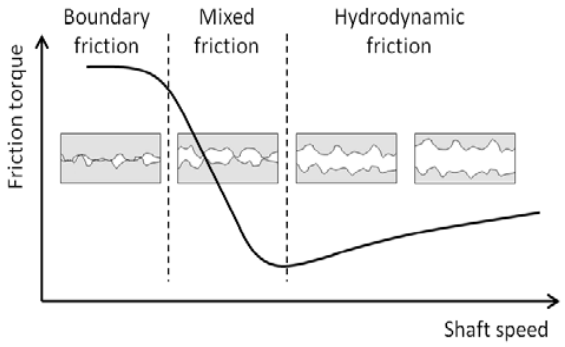

Figure 1: A Stribeck curve with different lubrication regimes (Sander et al. 2016).

There are several studies focusing on the influence of propeller-ice collisions on non-lateral propeller loads (i.e. torque and thrust). SAMPSON et al. (2013) describes that ice-induced propeller torque highly depends on the depth of cut of the ice. Ice-induced, lateral propeller loads are, however, discussed in only few studies. WANG et al. (2018) presented a numerical method to calculate lateral propeller loads due to ice milling. WANG et al. (2018) concluded that these loads are mainly influenced by the rotational speed of the propeller, feeding speed of the ice, size of ice floe and depth of cut. These influence factors mostly match the influence factors for non-lateral propeller loads presented by ZHOU et al. (2019) which suggests a correlation between lateral and non-lateral propeller loads induced by ice collisions. LEHMANN et al. (2022) therefore converted measured propeller torque (non-lateral load) during ice-collision events into a radial shaft force (lateral load) to investigate its influence on the propeller shaft bearings. On the basis of this work, the authors Gilges et al. (2023) studied the impact of propeller-ice collisions on the contact conditions within stern tube bearings and introduced a methodology for evaluating the associated wear risk. To achieve this, they categorized propeller torque and shaft RPM data collected during prior voyages of the SA Agulhas II during propeller-ice collisions. This classification served as the foundation for a combined approach, involving multibody and elasto-hydrodynamic simulations, to identify operating conditions that lead to a mixed-friction regime in the aft bearing. Their research unveiled critical operating conditions that result in a transition to a mixed friction regime in the aft bearing. Additionally, they presented a risk map which allows an evaluation of these operating conditions regarding their potential wear risk (see Figure 2).

The wear risk is indicated by the relative wear volume $V_{v,R}$. A value of 1 indicates operating conditions where wear is most likely to occur whereas a value of 0 means that wear does not occur in the absence of asperity contact. The presented method, however, neglects the influence of running-in wear on the contact conditions in the aft bearing (see Figure 3).

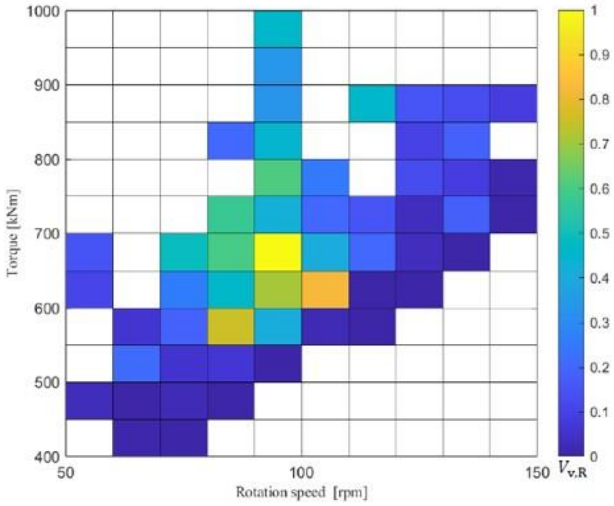

Figure 2: Risk map for the identification of wear-critical operating conditions (Gilges et al. 2023).

During the running-in phase, the wear rate shows a digressive behavior despite a constant load and rotational speed. This is due to the beneficial smoothing of surface roughness and contour of the bearing which leads to a reduction in asperity contact pressure. Only after that running-in phase a constant wear rate (steady state) can be assumed until reaching the progressive wear rate (wear out), right before catastrophic failure of the bearing. (Khonsari et al. 2021)

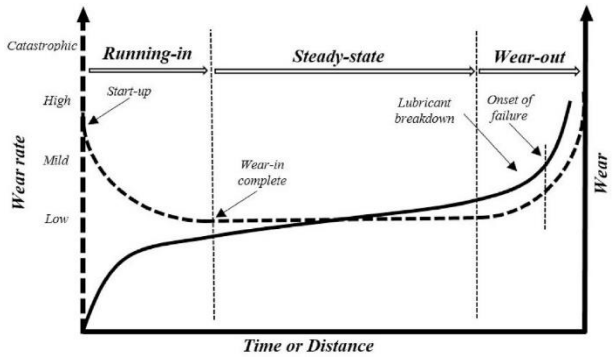

Figure 3: Schematic of the wear and wear rate behavior (Khonsari et al. 2021).

BARTEL et al. (2012), SANDER et al. (2016) & KÖNIG (2020) discuss the effects of surface smoothing caused by running-in wear on friction in dynamically loaded bearings. Their analysis considers changes in both surface roughness and bearing geometry and shows a significant reduction of the maximum contact pressure and friction in the bearing after completing the running-in phase. Hence, a method to include the influence of the running-in phase on the wear risk evaluation, shown in Figure 2, is required. This is necessary to accurately assess operating conditions during propeller-ice collisions regarding their wear risk potential for the aft bearing.

This study therefore focuses on an evaluation of the influence of the running-in phase in ship's stern tube bearings on wear risk during ice-collision loads. The research vessel SA Agulhas II is hereby used as a case study. Primary challenge is to develop a method to include

the surface roughness and contour adaption during the running-in phase in the wear risk assessment presented in Figure 2.

2 MATERIALS AND METHODS

The approach for the evaluation of wear critical operating conditions under consideration of the running-in surface adaptation is shown in Figure 4.

First, a laboratory-scale test rig, designed for investigating aft bearings, is used to determine the surface roughness adaptation during running-in phase for a preselected operating condition (see Section 2.1). Under the assumption, that the surface roughness change during running-in phase is load-case dependent, a method is needed to predict the surface roughness adaptation for changing operating conditions. Therefore, a combination of a numerical test rig model and a roughness wear algorithm is used (see Section 2.2). For model validation, the experimentally determined frictional torque, wear-induced changes of the test bearing contour and the surface roughness are used. To apply the roughness wear algorithm on vessel level, a scaling approach is developed which uses Fleischer's wear model (see Section 2.3). Following, the roughness of the aft stern tube bearing, after completing the running-in phase, is determined by applying the roughness wear algorithm on vessel level for a design load case. Finally, an assessment of the impact of the running-in phase on the wear behavior of the aft bearing is carried out. Therefore, a new risk map is derived on the basis of the methodology presented in the previous work of the authors (Gilges et al. 2023) (see Subsection 2.4).

2.1 Journal bearing test rig

For the experimental investigation of the wear behavior in aft stern tube bearings, a test rig was designed (see Figure 5). As the original aft bearing diameter of the SA Agulhas II is 570 mm, a down-scaled test rig design (Geometry scaling factor: 12.67) was chosen, to ensure economic feasibility of the tests.

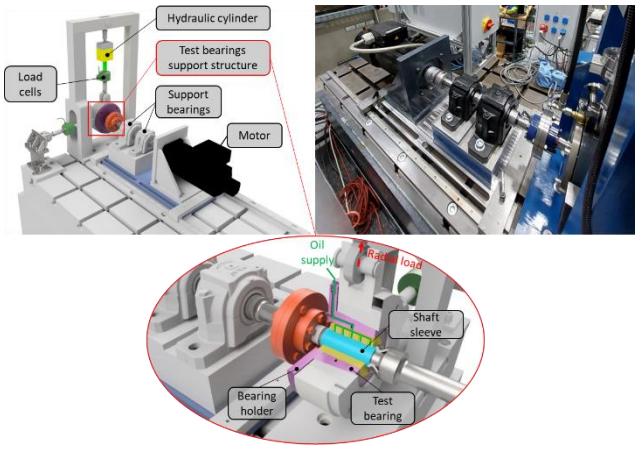

Figure 4: Aft stern tube bearing test rig.

2.1.1 Test rig specifications

The designed test rig consists of a 20 KW Motor, two support bearings (spherical roller bearings), a test bearing with a support structure and a hydraulic cylinder for direct application of a radial load. The test bearing is constantly supplied with oil by a recirculating lubrication system. The temperature of the oil can be manually set by the operator. During operation of the test rig, radial load, rotational shaft speed, friction torque, bearing temperature and oil inlet temperature are measured.

To ensure comparability between the test rig results and the original bearing in the vessel, the bearing geometry, material and operating conditions need to be properly scaled. For geometric down scaling, similarity parameters were used such as ratio of bearing width W to bearing diameter D (W/D ratio) and relative bearing clearance ψ. Material parameters such as bearing coating material, coating thickness, shaft material and lubricant were selected to be as close as possible to the original design. The respective geometry and material parameters are shown in Table 1. The scaling of the bearing operation is described in Section 2.3.

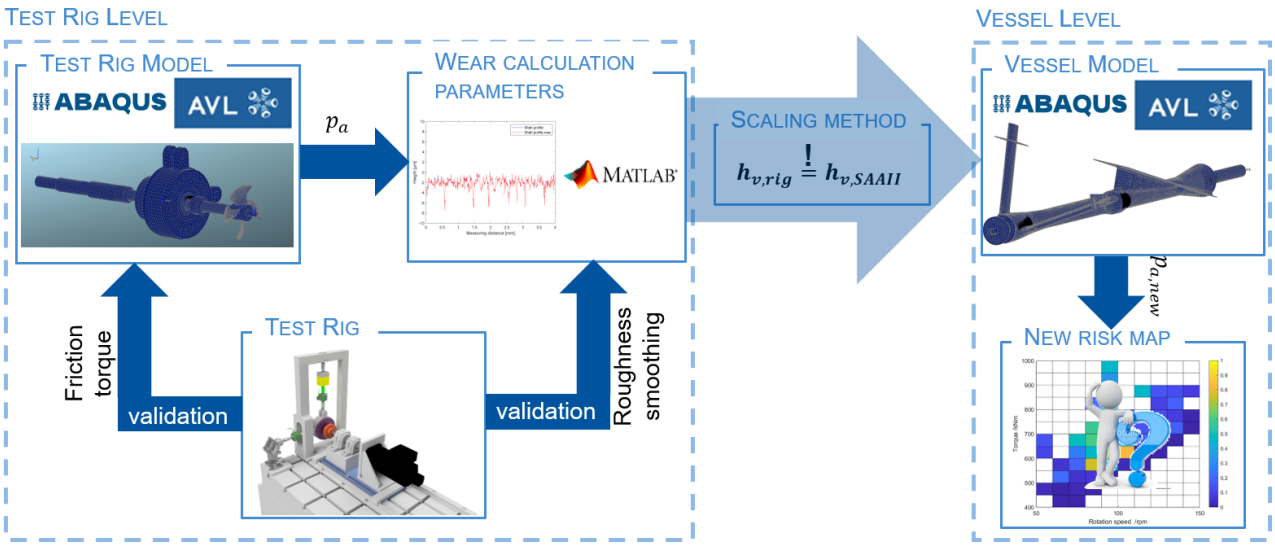

Figure 5 Schematic depiction of the approach for the evaluation of wear critical operating conditions including the running-in phase of the bearing.

Table 1: Geometry and material parameters of the test bearing-sleeve combination

Parameters	*Values*
Geometry scaling factor	12.67
Inner bearing diameter	45 mm
W/D ratio	2
Relative bearing clearance	1.4 h
Bearing coating material	PbSb15Sn10
Coating thickness	4 mm
Shaft sleeve material	42CrMo4
Lubricant	Castrol BioStat 100

2.1.2 Test conditions

The test rig employed in this study serves a dual purpose: (1) Validation of numerical model (Validation test) and (2) Quantification of wear development and roughness adaptation during running-in phase (Running-in test). To validate the numerical test rig model, the development of friction torque over changing rotational speeds (Stribeck curve) for both test rig and numerical test rig model is compared. Figure 6 shows the test procedure for the experimental validation test.

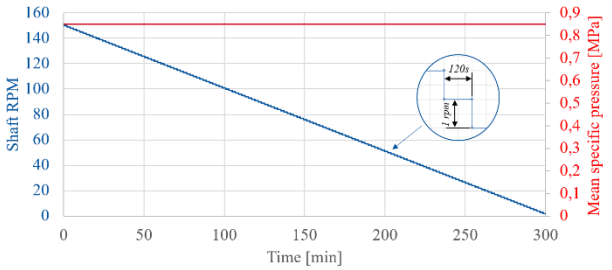

Figure 6: Test procedure for the validation test of the numerical test rig model.

A constant load of 0,86 MPa was applied to the bearing and the rotational speed was gradually decreased from 120 rpm to 0 rpm in increments of 1 rpm. The holding time in between the rpm steps was set to 120 seconds to account for transition-effects (e.g. settling of the motor speed after a speed change) when changing the rotational speed. Figure 7 shows the procedure for the running-in tests.

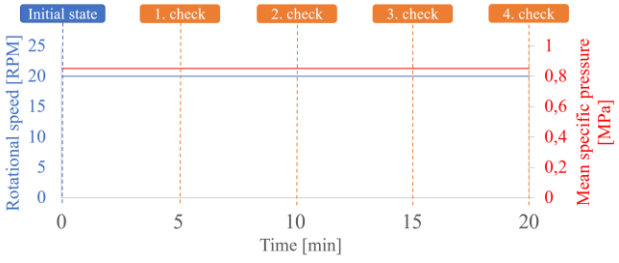

Figure 7: Test procedure for the running-in test.

Same as for the validation tests, a constant load of 0,86 MPa was applied. This ensures applicability of the validated model to the running-in tests. The rotational speed was set to a constant value of 20 rpm which, according to the numerical test rig model, leads to a mixed-friction operation for the chosen bearing-shaft combination. To capture the change in surface roughness, the bearing was disassembled after every 5 minutes of operation. After every disassembly, both contour and surface roughness were measured. The iterative testing process persisted until the surface roughness of the bearing reached its minimum attainable value which indicates the end of the running-in phase.

2.2 Numerical Simulation

For the simulation, the commercial software AVL Excite Power Unit was employed. This software couples elasto-hydrodynamic (EHD) simulation with multi-body system (MBS) analysis, considering temperature and pressure-dependent fluid properties, cavitation, structural deformation, and the effects of hydrodynamics and frictional work on the surface (AVL-List GmbH, Lehmann et al. 2022). The software was used to conduct isothermal simulations of both the stern tube arrangement of the SA Agulhas II and the test rig. The stern tube model encompassed the stern tube shaft, the three stern tube sliding bearings (aft, middle and forward bearing) and the surrounding support structure, as depicted in Figure 8.

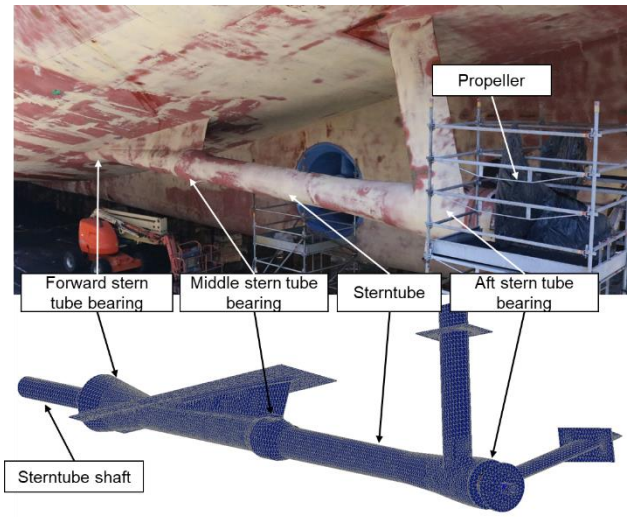

Figure 8: Model of the drive train of the SA Agulhas II research vessel.

The test rig model was developed to replicate the loading conditions experienced by the test bearing within the test rig. This model consisted of six components (refer to Subsection 2.1): the test bearing, the test bearing support structure, the drive shaft, the motor shaft and the support bearings, all shown in Figure 9. A detailed description of the applied simulation approach used for both vessel level and test rig level is presented in Subsection 2.2.1. Following this, the wear calculation and the roughness wear algorithm are thoroughly discussed in Subsection 2.2.2.

2.2.1 Simulation approach

In the modeling approach used in the excite software, the nonlinear mechanical system is divided into subsystems. These subsystems own both nonlinear behavior represented by elasto-hydrodynamic sliding bearing contact and linear elastic behavior represented by the drive shaft, surrounding support structure and connection to the hull (AVL-List GmbH, Lehmann et al. 2022, Gilges et al.

2023). In this study, isothermal elasto-hydrodynamic simulations were conducted based on the average Reynolds equation.

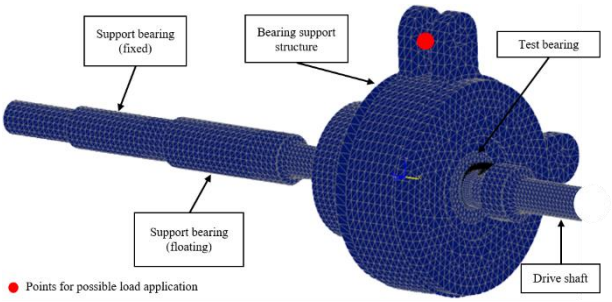

Figure 9: Test rig model.

To describe the asperity-contact behavior, the model according to GREENWOOD and TRIPP (1970) was used. The Reynolds equation is therefore given as:

$$\frac{\partial}{\partial x}\left(h^3\frac{\partial p}{\partial x}\right)+\frac{\partial}{\partial y}\left(h^3\frac{\partial p}{\partial y}\right)=6\eta\frac{\partial U}{\partial h}\frac{\partial h}{\partial x}+12\eta\frac{\partial h}{\partial t} \qquad (1)$$

In equation 1, x and y correspond to the length and width directions, while h represents the local lubricant film thickness, which depends on both x and y. The variable p signifies the hydrodynamic pressure. When calculating the total velocity U based on surface velocities in the longitudinal direction, there is no coupling with the energy equation, a common practice in hydrodynamics. Consequently, thermal effects such as variations in viscosity or density due to temperature changes are not considered. By characterizing the considered fluids as Newtonian fluids, the viscosity μ does not depend on the shear rate and thus remains constant (König 2020).

The simulation considers the influence of surface roughness on hydrodynamic lubrication by employing the averaged Reynolds equation, as outlined by PATIR and CHENG (1978, 1979). Nevertheless, it has been noted that the effects of pressure and shear flow factors on friction power losses are minimal within the examined operating conditions (Sander et al. 2015, Sander et al. 2016).

The friction torque acting on the bearing surface, which is employed as a validation parameter for the simulation model, results from a combination of hydrodynamic losses and losses attributed to asperity contact (Sander et al. 2015, Sander et al. 2016, Allmaier et al. 2011, Allmaier et al. 2012). Consequently, the friction torque M_{Friction} can be determined by integrating the shear stresses across the bearing surface:

$$M_{\mathrm{Friction}}=\int Shear\ Stresses\ dA \qquad (2)$$

The hydrodynamic shear stresses are determined using shear stress factors according to PATIR and CHENG, while the shear stress arising from asperity contact is calculated based on the asperity contact pressure and a literature-based friction coefficient (Sander et al. 2015, Sander et al. 2016, Allmaier et al. 2011, Allmaier et al. 2012). The asperity contact pressure is determined through the GREENWOOD and TRIPP approach (1970).

2.2.2 Wear calculation and roughness wear algorithm

For the wear calculation, the model for the wear depth h_v according to FLEISCHER et al. (1980) was used (see Equation 3).

$$h_{\mathrm{v,Fleischer}}=\frac{\int F_{\mathrm{R}}\,ds_{\mathrm{R}}}{e^*_{\mathrm{R}}.A_{\mathrm{a}}}.T_{acc}=\frac{\mu}{e^*_{\mathrm{R}}}.p_{\mathrm{a}}.s_{\mathrm{R}} \qquad (3)$$

F_R is the asperity contact force, s_R is the sliding distance, e_R^* is the apparent friction energy density, A_a is the asperity contact area, T_{acc} is the total accumulation time, p_a is the asperity contact pressure, and μ is the friction coefficient. The apparent frictional energy density along with the friction coefficient can be determined experimentally for a specific material combination and lubrication. The asperity contact pressure p_a can be determined by means of the numerical simulation (see Section 2.2). The pressure p_a, however, changes continuously during the running-in phase of the bearing due to the chaining surface roughness. A changing asperity contact pressure leads to a changing development of the wear depth h_v. Hence, the calculation of the wear depth and surface roughness change during the running-in phase have to be conducted iteratively. The iteration approach for the roughness wear, used in this study, is based on the work of KÖNIG (2019, 2020). The starting point for the iteration is represented by the pre-operation state of the test bearing (new bearing). The measured roughness of the new bearing is used as an input for the simulation model to calculate the resulting asperity contact pressure for the given load conditions and time step size of the running-in tests (see Subsection 2.1.2). By means of the asperity contact pressure and the experimentally determined apparent frictional energy density, the new surface roughness is estimated. For the new surface roughness, the process was repeated until reaching the same wear depth as in the running-in tests at the end of the running-in phase.

2.3 Scaling method for bearing wear

To apply the wear calculation and roughness wear algorithm to the numerical model on vessel level, a scaling method was developed. This scaling method is based on FLEISCHER's wear model (see Equation 3). This scaling method aims to achieve equality in wear depth between the test bearing (at the test rig level) and the aft bearing of the ship (at the vessel level) during mixed friction operation, as shown in Equation 4.

$$h_{\mathrm{v,Vessel}}=h_{\mathrm{v,Testrig}} \qquad (4)$$

According to FLEISCHER (as shown in Equation 3), the wear depth h_v is influenced by several factors, including the friction coefficient μ, sliding distance s_R, asperity contact pressure p_a, and apparent frictional energy density e_R^*.

Equality for the friction coefficient μ in mixed friction regime is assumed for using identical material combinations, surface roughnesses, lubricant and temperature. Equality for the sliding distance s_R can be reached by adjusting the testing time. Equality in asperity contact pressure p_a can be reached by adjusting the radial

bearing load and rotational speed of the tests (Greenwood & Tripp, 1970). The apparent frictional energy density depends on the number of contacts until failure n_k, average fracture energy density $\bar{e}_b$, energy accumulation number $\zeta_R$and wear number v_v, as shown in Equation 5.

$$e_{\mathrm{R}}^{*} = \frac{n_{\mathrm{k}}}{v_{\mathrm{v}}} \cdot \frac{\bar{e}_{\mathrm{b}}}{1 + \zeta_{\mathrm{R}} \cdot (n_{\mathrm{k}} - 1)} \tag{5}$$

The parameters that influence the wear depth and their corresponding dependencies are summarized in Table 2. The apparent frictional energy density e_R^* is mainly dependent on material properties and asperity contact pressure. By choosing the same bearing and shaft material combination with the same material properties and contact pressure, for vessel and test rig, equality can be assumed for the number of contacts until failure n_k, average fracture energy density e_{b} and energy accumulation number ζ_R. Only for the wear number v_v (see Equation 6), the contact geometry (radius of the unevenness r, asperity contact area A_r and number of asperity contacts j_r) has an influence:

$$v_{\mathrm{v}} = \frac{h_{\mathrm{v}}}{h_{\mathrm{R}}} \tag{6}$$

with

$$h_{\mathrm{R}} \approx 2 \cdot r_0 = 2 \cdot \sqrt[3]{\frac{3}{4} \cdot \frac{r \cdot F_{\mathrm{k}}}{E_{\mathrm{red}}}} \tag{7}$$

To reach equality of the wear number v_v between test rig level and vessel level, equality for the wear depth h_v and the stress depth h_R needs to be achieved. The wear depth is the resulting parameter of interest and is thus assumed to be equal for test rig and vessel level. The stress depth h_R depends on various parameters (see Equation 7. For the radius of the unevenness r and the reduced young's modulus E_{red} equality can be assumed for the same surface roughness and material properties. The normal force related to the number of contact points F_k depends on asperity contact pressure, area and number of asperity contacts:

$$F_{\mathrm{k}} = \frac{p_{\mathrm{a}} \cdot A_{\mathrm{r}}}{j_{\mathrm{r}}} \quad \& \; A_{\mathrm{r}} \propto j_{\mathrm{r}} \tag{8}$$

When assuming equality for the asperity contact pressure, the contact area changes with the geometrical down-scaling of the bearing. Because of the proportionality between asperity contact area A_r and number of asperity contacts j_r, the resulting force F_k is, however, assumed to stay the same.

Building upon the prior elaborations and assumptions, equality between test rig and vessel level can be reached for all the influence parameters of the wear depth. Thus, the wear calculation and roughness wear algorithm which is validated on test rig level can be applied on vessel level. This allows the calculation of the running-in geometry for the aft bearing of the SA Agulhas II without conduction measurements of that bearing during its running-in phase. Subsequently, this approach allows an improvement of a risk map by including the bearing surface adaptation during the running-in phase to the analysis of wear-critical operating conditions (see Section 2.4).

2.4 Risk Map of the wear-critical operating conditions

To generate a risk map, highlighting wear-critical operating conditions, the same methodology as presented in the previous publication (Gilges et al. 2023) is used. As an improvement, the surface adaptation due to the running-in phase of the aft bearing is included by applying the method presented in Section 2.2. Using the wear depth and asperity contact area, both determined from the simulation, sliding distance and the maximum asperity pressure, the wear volume V_v can be calculated. The wear volume V_v can then be normalized to a relative wear volume $V_{v,R}$ (see Equation 9) to finally merge the wear-critical operating conditions in a risk map.

$$V_{\mathrm{v,R}} = \frac{V_{\mathrm{v}}}{\max(V_{\mathrm{v}})} \tag{9}$$

To evaluate to influence of the running-in phase on the risk map, the percentage deviation $V_{v,R,dev}$ of the wear risk was used. $V_{v,R,dev}$ compares the relative wear volume considering the running-in phase $V_{v,R,run}$ with the relative wear volume without consideration of the running-in phase $V_{v,R}$:

$$V_{\mathrm{v,R,dev}} = \frac{V_{\mathrm{v,R,run}} - V_{\mathrm{v,R}}}{V_{\mathrm{v,R}}} \tag{10}$$

3 RESULTS AND DISCUSSION

This section begins in subsection 3.1 with a comparison between measurement and simulation results to validate the test rig model. Subsequently, subsection 3.2 discusses

Table 2: Influences on wear depth according to FLEISCHER model

Parameter	*Description*	*Influenced by*
μ	Friction coefficient	Material properties, lubrication
p_{a}	Asperity contact pressure	Experimental test procedure
S_{R}	Sliding distance	Experimental test procedure
e_{R}	Apparent frictional energy density	
n_{k}	Number of contacts until failure	Material properties, asperity contact pressure
$\bar{e}_{\mathrm{b}}$	Average fracture energy density	Material properties
ζ_{R}	Energy accumulation number	Material properties, loading
v_{v}	Wear number	
h_{v}	Wear depth	wanted parameter
r	Radius of the unevenness	Surface roughness
E_{red}	Reduced young's modulus	Material properties
F_{k}	Normal force related to the number of contact points	Asperity contact pressure, area and number

the running-in results on test rig level. Finally, subsection 3.3 shows the running-in results on vessel level followed by the presenting operating parameter risk map including the running-in phase of the aft bearing.

3.1 Validation of the simulation model

To validate the simulation model of the test rig, the experimental determined development of the friction torque over the rational speed (Stribeck curve) can be used (Sander et al. 2016). Figure 10 shows a comparison between measured and calculated friction torque. The blue curve represents the calculated friction torque from test rig simulation model. The black curve shows the average of the measured friction torque during the validation test. The grey area represents the uncertainty band of the torque and speed measurements.

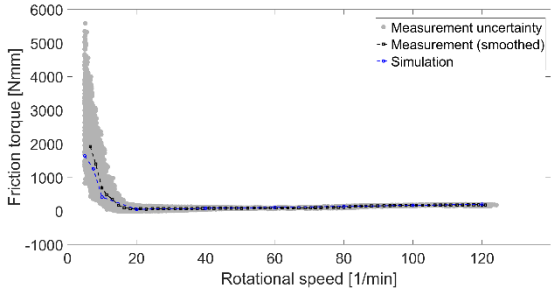

Figure 10: Stribeck curve: simulation vs. measurement of validation test

The results reveal that when operating above 20 rpm with the hydrodynamic regime, both the measured and calculated friction torque are nearly identical. However, below 20 RPM or within the mixed friction regime, the deviation between the measured and calculated friction torque noticeably increases. This deviation may arise from inaccuracies in the torque and speed measurements, as well as the surface roughness measurements, since they directly influence the contact model according to Greenwood and Tripp's approach (1970). The maximum absolute deviation is 614.8 Nmm for 7 rpm and it is decreasing for increasing rotational speed. Especially for rotational speeds below 13 rpm the model shows potential for optimization. For rotational speeds near 20 rpm and during mixed friction operation, both model and experimental results match very well.

Hence, it can be concluded that both the simulation approach and the test rig model are valid for operating conditions in fluid friction regime and operating conditions in mixed-friction regime, near the transition point to fluid friction (at 20 rpm). Subsequently, this simulation model is further employed for the development of wear calculation and roughness wear algorithms through wear tests.

3.2 Running-in results on test rig level

The running-in tests were carried out corresponding to the test procedure presented in Figure 7. During the first 20 minutes of tests, the surface roughness of the test bearing decreased monotonously. After 20 minutes, the roughness did not reduce further which indicates the end of the running-in phase. Figure 11 shows the test bearing after completing the running-in phase.

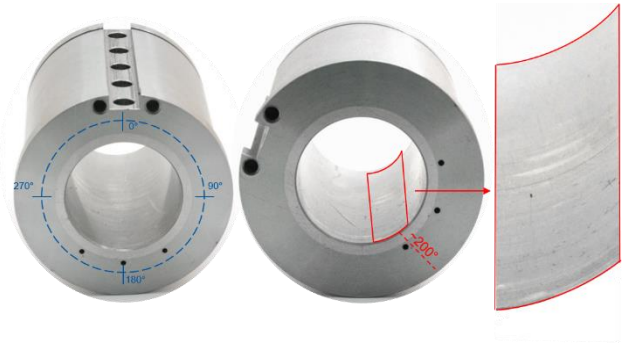

Figure 11: Test bearing after 20 minutes of running-in test.

The most noticeable running-in wear occurs at around 200° of circumferential position which represents the loading zone of the bearing. Within the loading zone, the wear depth $h_{v,Testing}$ was calculated on the basis of roundness measurements of the test bearing (before and after the running-in tests). The procedure for the determination of the wear depth is based on the approach presented by BOTE-GARCIA and GUHMANN (2021). The roundness was measured over 14 equidistant positions over the bearing width and then averaged (within the loading zone of 200°) to a wear depth value $h_{v,Testing}$ of 0.1845 µm. Figure 12 shows the simulated wear over bearing width and circumferential bearing angle of the test rig model.

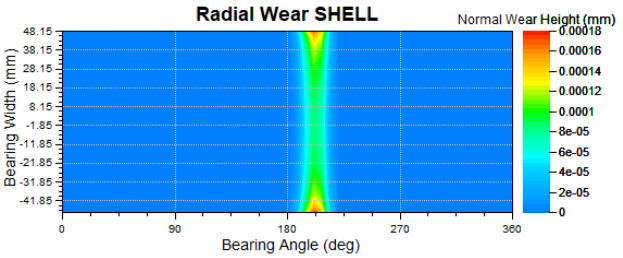

Figure 12: Simulated wear depth distribution after 20 minutes of running-in test.

The circumferential position (at 200°) of the occurring wear resulting from the simulation matches very well the load zone position of the test bearing (see Figure 11). The wear depth of the simulation extends over the entire bearing width and has its maximum value at the bearing edges. This could be due to a load induced bending of the shaft.

By means of Equation 3, the apparent frictional energy density e_R^* of 0.45 $\cdot 10^{14}$ J/m^3 was calculated. The necessary asperity contact pressure was determined by means of the test rig simulation model, the friction coefficient was derived from the measured friction torque and the sliding distance was calculated from the rotational speed of the shaft.

On the basis of the wear depth and the roughness wear algorithm, the surface roughness change was determined. Figure 13 shows the normalized roughness development Ra* and Rq* during the running-in phase for both experimental and simulative approach.

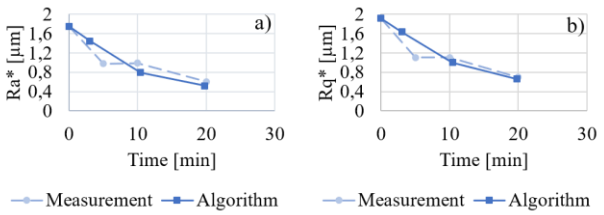

Figure 13: Roughness development a) Ra* and b) Rq* for the measurements of running-in tests and the results of the roughness wear algorithm.

It is noticeable that the roughness curves match quite well. For the resulting roughness after 20 minutes, the results from the algorithm differ 5.2% for Ra* and 1.8% for Rq* from measurements. Figure 14 shows the development of the peak contact pressure over time. The shown contact pressure values were used as input for the iteration steps of the roughness wear algorithm.

Overall, the peak asperity contact pressure in the test bearing reduces from 2.7 MPa to 0.6 MPa due to the smoothing in of the surface roughness. In the next step, the model approach was applied on the vessel level.

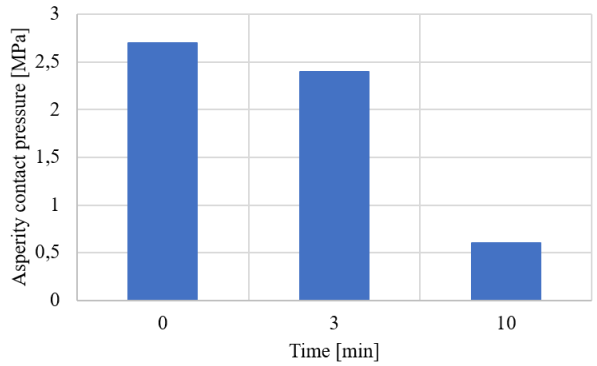

Figure 14: Development of the peak asperity contact pressure for resulting from roughness algorithm

3.3 Running-in results on vessel level and risk map

After achieving equality in wear depth between the test rig level and the vessel level (see Section 2.3), the developed wear calculations and roughness wear algorithms can be applied to the stern tube model of the SA Agulhas II to obtain the surface roughness of the aft bearing after the running-in phase. Therefore, a design load case with an ice torque of 1009 kNm and rotational speed of 140 rpm as per the design specifications by DNV was employed (Purcell et al. 2021). This load case is used as it represents a worst-case scenario and it is employed in the design process of most vessels operating in ice-covered waters. As previously discussed in Section 2.1.2, the achievement of the minimum attainable and constant surface roughness value serves as the criterion to validate the successful completion of the running-in phase. Figure 15 illustrates the development of the normalized surface roughness Rq* during the running-in process for the DNV design load case. The running-in phase lasts only 4.2 seconds consisting of 6 iterations. This short amount of time may be due to the extraordinary high load (1009 kNm) of the used design load case.

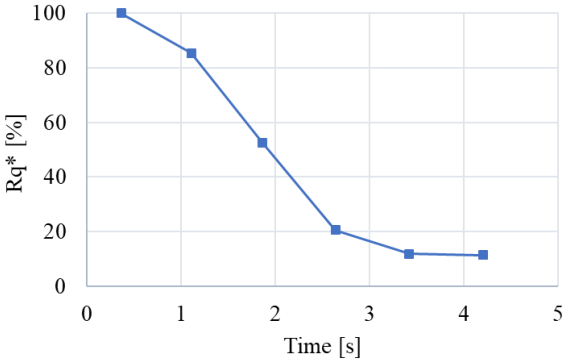

Figure 15: Roughness development Rq* for the aft bearing (vessel level) during the running-in phase

Using the obtained roughness data from the simulated running-in phase and considering the operating conditions as per (Gilges et al. 2023), simulations were conducted to identify the wear risk for different operating conditions for the aft bearing with completed running-in phase. For the identified operating conditions, the wear volumes were calculated. Hereby the wear depth and asperity contact area, obtained from the simulation, and the sliding distance resulting from the load frequency and load time were used. Based on the wear volumes by the resulting ice-induced propeller loads, a risk map was generated in order to identify the wear-critical operating conditions (see Figure 16). The relative wear volume $V_{v,R}$ was calculated according to Equation 9.

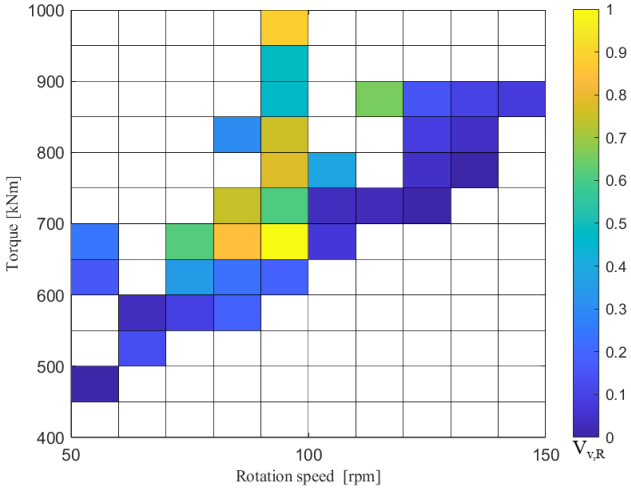

Figure 16: Risk map for the identification of wear-critical operating conditions including the running-in Phase of the bearing.

The highest wear risk occurs for a rotational speed of 90-100 rpm and an ice-induced propeller torque of 650-700 kNm. Torque values for rotational speeds below 80 and above 120 show a low wear risk which is due to a low occurrence frequency of these load cases.

3.4 Assessment of running-in phase on wear development (Risk Map)

Figure 17 shows the deviation of wear risk for consideration and non-consideration of the running-in phase of the bearing. Hereby, the percentage deviation $V_{\mathrm{v,R,dev}}$ over the operating conditions of the aft bearing was

used (see Section 2.4). The impact of the running-in process on the risk map is contingent on variations in torque and speed. When torque decreases or speed increases (i.e. lower asperity contact pressure), especially near the transition point from mixed-friction to fluid-friction regime, the influence of the running-in phase becomes significant. Conversely, under conditions of higher contact pressure, the running-in phase exerts minimal influence on the resulting wear risk.

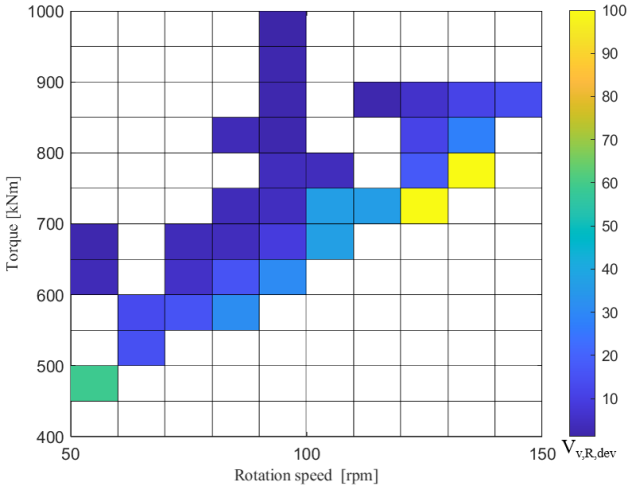

Figure 17: Deviation of wear risk for consideration and non-consideration of the running-in Phase

The presented risk map with consideration of the running-in phase of the bearing (see Figure 16) can serve as a foundational tool for formulating ship operator guidelines and maintenance plans for vessel operations in ice-covered waters. This implies that, for instance, by a propeller torque between 650-700 kNm and a rotational speed between 90-100 rpm, increasing the rotational speed by 20% ensures safe operations.

4 CONCLUSION

The aim of this study was to assess the influence of the running-in phase in ship's aft bearing on the wear development during ice-collision loads. In this work, a novel approach to calculate the running-in wear in the aft bearing of the SA Agulhas II on the basis of down-scaled experiments and numerical simulation models was introduced. With this approach, the running-in wear could be included in the wear assessment of the operating conditions during propeller-ice collisions. Based upon the results obtained, the following conclusions can be drawn:

1. The surface roughness adaptation due to the running-in phase of the aft bearing lead to a reduction of the asperity contact pressure in mixed friction regime.
2. The influence of the running-in phase on the wear risk is significant for operating conditions close to the transition line from mixed friction to fluid friction regime. For operating conditions deep within the mixed-friction regime (i.e. for high asperity contact pressures) the influence of the running-in phase on the wear risk is almost negligible.
3. A risk map with consideration of the running-in phase was presented that identifies wear critical operating conditions for the aft bearing under propeller-ice collisions. This risk map can thus serve as a foundation for operator guidance and maintenance plans for safe vessel operation in ice-covered waters. For instance, by a propeller torque between 650-700 kNm and a rotational speed between 90-100 rpm, increasing the rotational speed by 20% ensures safe operations.

ACKNOWLEDGEMENTS

The authors would like to acknowledge support from MarTERA - an ERA-NET Cofund scheme of Horizon 2020 of the European Commission - and the Research Council of Norway (Project no. 311502), the Federal

Ministry for Economic Affairs and Climate Action of Germany (Project no. 03SX519B), and Department of Science and Technology of South Africa, through the HealthProp project.

REFERENCES

Allmaier, H., Priestner, C., Reich, F. M., Priebsch, H. H., Forstner, C., Novotny-Farkas, F. (2012). 'Predicting friction reliably and accurately in journal bearings – the importance of extensive oilmodels'. Tribology International 48: pp. 93–101.

Allmaier, H., Priestner, C., Six, C., Priebsch, H. H., Forstner, C., Novotny-Farkas, F. (2011). 'Predicting friction reliably and accurately in journal bearings—a systematic validation of simulation results with experimental measurements'. Tribology International 44(10): pp. 1151–1160.

AVL-List GmbH (2022). Excite power unit user manual (2022.1).

Bartel, D., Bobach, L., Illner, T., Deters, L. (2012). 'Simulating transient wear characteristics of journal bearings subjected to mixed friction'. Proceedings of the Institution of Mechanical Engineers Part J: Journal of Engineering Tribology 226(12): pp. 1095–1108.

Bote-Garcia, J.-L. & Guhmann, C. (2021). 'Schaetzung des Verschleißvolumens an Gleitlagern'. tm - Technisches Messen 88(s1): pp. s17–s21.

DNV AS (2022). Safeguard shaft seals and propeller shaft bearings – avoid costly failures.

Fleischer G., Groger H., Thum H. (1980). Verschleiß und Zuverlassigkeit. VEB Verlag Technik, Berlin.

Frame, B., Liggett, D., Lindstrom, K., Roura, R. M., van der Watt, L.-M. (2022), 'Tourism and heritage in antarctica: exploring cultural, natural and subliminal experiences'. Polar Geography, 45(1): pp. 37–57.

Gilges, M., Saleh, A., Jain, M., Bekker, A., Lehmann, B., Jacobs, G. (2023). 'Influence of propeller-ice loads on the wear development in stern tube bearings of marine propulsion systems and identification of critical operating conditions'. Proceedings of the ASME 2023 42nd International. Conference on Ocean, Offshore and Arctic Engineering, OMAE2023.

Greenwood, J. A. & Tripp, J. H. (1970). 'The contact of two nominally flat rough surfaces'. Proceedings of the Institution of Mechanical Engineers 185(1): pp. 625–633.

Hagesteijn, G., Brouwer, J., and Bosman, R. (2012). 'Development of a six-component blade load measurement test setup for propeller-ice impact'. Materials Technology; Polar and Arctic Sciences and Technology; Petroleum Technology Symposium. Volume 6: pp. 607–616. American Society of Mechanical Engineers.

He, T., Zhu, D., Wang, J., Jane Wang, Q. (2017). 'Experimental and numerical investigations of the stribeck curves for lubricated counterformal contacts'. Journal of Tribology 139(2).

Khonsari, M. M., Ghatrehsamani, S., Akbarzadeh, S. (2021). 'On the running-in nature of metallic tribo-components: A review'. Wear 474-475.

Koenig F. (2020). Prognose des Verschleißverhaltens ölgeschmierter Gleitlager im Mischreibungsbetrieb. Verlagsgruppe Mainz GmbH, Aachen.

Koenig, F., Ouald Chaib, A., Jacobs, G., Sous, C. (2019). 'A multiscale-approach for wear prediction in journal bearing systems – from wearingin towards steady-state wear'. Wear 426-427: pp. 1203–1211.

Lehmann, B., Gutierrez Guzman, F., Jacobs, G. (2022). 'Einfluss von Eiskollisionslasten am Propeller auf die Kontaktzustande in den Antriebsstranggleitlagern von Schiffen'. Tribologie und Schmierungstechnik 69(3): pp. 5–17.

Patir, N. & Cheng, H. S. (1978). 'An average flow model for determining effects of three-dimensional roughness on partial hydrodynamic lubrication'. Journal of Lubrication Technology 100(1): pp. 12– 17.

Patir, N. & Cheng, H. S. (1979). 'Application of average flow model to lubrication between rough sliding surfaces'. Journal of Lubrication Technology 101(2): pp. 220–229.

Purcell, E., Nejad, A. R, Valavi, M., Bekker, A. (2021) 'On uncertainty assessment of fatigue damage of propulsion shaft under ice impact'. Proceedings of the ASME 2021 40th International, Conference on Ocean, Offshore and Arctic Engineering. OMAE2021.

Sampson R., Atlar M., John J.W. St, Sasaki N. (2013). 'Podded propeller ice interaction in a cavitation tunnel'. Proceedings of the Third International Symposium on Marine Propulsors SMP. Launceston, TAS, Australia.

Sander, D. E., Allmaier, H., Priebsch, H. H., Reich, F. M., Witt, M., Fullenbach, T., Skiadas, A., Brouwer, L., Schwarze, H. (2015). 'Impact of high pressure and shear thinning on journal bearing friction'. Tribology International 81: pp. 29–37.

Sander, D. E., Allmaier, H., Priebsch, H. H., Witt, M., Skiadas, A. (2016). 'Simulation of journal bearing friction in severe mixed lubrication – validation and effect of surface smoothing due to runningin'. Tribology International 96: pp. 173–183.

Spikes, H. A. (1997). 'Mixed lubrication — an overview'. Lubrication Science 9(3): pp. 221–253.

Sugimura, T., Yamaguchi, H., Yabuki, H. (2021). 'Development and implementation of an arctic sea route search system'. Polar and Arctic Sciences and Technology. Volume 7, American Society of Mechanical Engineers.

Vartdal B., Gjestland T., and Arvidsen T. (2009). 'Lateral propeller forces and their effects on shaft bearings'. First International Symposium on Marine Propulsors. Trondheim, Norway.

Wang, C., Xiong, W. P., Chang, X., Ye, L. Y., Li, X. (2018). 'Analysis of variable working conditions for propeller-ice interaction'. Ocean Engineering 156: pp. 277–293.

Zhou L., Wang F., Diao F., Ding S., Yu H., Zhou Y. (2019). 'Simulation of ice-propeller collision with cohesive element method'. Journal of Marine Science and Engineering 7(10): p. 349.